Christopher A. Cameron, David R. Allan, Konstantin V. Kamenev, Stephen A. Moggach, Mark Murrie and Simon Parsons*

A pressure-induced displacive phase transition in Tris(ethylenediamine) Nickel(II) nitrate

Abstract: $[Ni(en)_3][NO_3]_2$ undergoes a displacive phase transition from $P6_322$ at ambient pressure to a lower symmetry $P6_122/P6_522$ structure between 0.82 and 0.87 GPa, which is characterized by a tripling of the unit cell *c*-axis and the number of molecules per unit cell. The same transition has been previously observed at 108 K. The application of pressure leads to a general shortening of O ... H hydrogen bonding interactions in the structure, with the greatest contraction (24%) occurring diagonally between stacks of Ni cation moieties and nitrate anions.

Keywords: phase transition, high pressure, synchrotron radiation, coordiniation chemistry

*Corresponding Author: **Simon Parsons,** EaStCHEM School of Chemistry and Centre for Science at Extreme Conditions, The University of Edinburgh, King's Buildings, West Mains Road, Edinburgh, Scotland, EH9 3JJ, e-mail: s.parsons@ed.ac.uk
Christopher A. Cameron, Stephen A. Moggach: EaStCHEM School of Chemistry and Centre for Science at Extreme Conditions, The University of Edinburgh, King's Buildings, West Mains Road, Edinburgh, Scotland, EH9 3JJ
David R. Allan: Diamond Light Source, Harwell Science and Innovation Campus, Chiltern, Didcot, Oxfordshire OX11 0QX
Konstantin V. Kamenev: School of Engineering and Centre for Science at Extreme Conditions, The University of Edinburgh, King's Buildings, West Mains Road, Edinburgh, Scotland, EH9 3JZ
Mark Murrie: School of Chemistry, University of Glasgow, Glasgow, Scotland, G12 8QQ

1 Introduction

Ethylenediamine is one of the most common bidentate ligands used in coordination chemistry. When coordinated to a metal centre it forms a five-membered ring which offers increased stability over similar monodentate ligands, and analysis of this effect played an important role in the understanding of metal-ligand coordination.

The crystal structure for $[Ni(en)_3][NO_3]_2$ was first obtained by Swink and Atoji (Cambridge Database refcode = TEANIN) [1]. These studies determined that under ambient conditions the crystal structure consisted of two formula units in a hexagonal unit cell where $a = b = 8.87(1)$ Å and $c = 11.41(2)$ Å. The nickel cation has an approximately octahedral geometry but skewed due to non-90° N–Ni–N angles with the ligands adopting a *gauche* conformation. Extensive bifurcated hydrogen bonding networks were observed involving ethylenediamine hydrogen atoms and nitrate oxygen atoms, which helped stabilize the close proximity of the two staggered nitrate anions. The structure has been most recently determined by Macchi et al. [2], who analysed the effect of microsource Mo X-ray radiation on crystal data quality.

Molecular materials are very susceptible to changes in temperature and pressure due to the relatively weak nature of intermolecular interactions [3]. The accuracy and precision of data collections can also be significantly improved through the application of low temperature conditions [4]. Consequently there is increasing interest among researchers in utilizing temperature and pressure to analyse the solid state [5]. The earliest crystal structure determination of $[Ni(en)_3][NO_3]_2$ at low-temperatures was conducted by Farrugia et al. [6], with the goal of investigating the electron density distribution. In the process the researchers discovered a phase transition occurring at 109 K from the $P6_322$ ambient phase to a new $P6_522$ phase, where $a = b = 8.82020(10)$ Å, $c = 33.1447(4)$ Å, and $V = 2233.07(4)$ Å^3. The enlargement of the unit cell through tripling of the *c*-axis coincided with an increase in *Z* from 2 to 6, caused by a displacement of the nickel cations towards a position of lower symmetry. This transition was discovered to be sharp and reversible, as well as easily observable in precession images, making the compound ideal as a low-temperature calibrant for cryostats.

Pressure is a highly efficient variable for probing the structure of materials: unlike temperature which can typically be varied by up to a few hundred Kelvin for molecular materials, modern apparatus is capable of generating many billions of Pascals, resulting in far greater changes in crystalline thermodynamics [7]. Additionally the phase changes induced by pressure may be very different to those caused by temperature, generating interest into the reasons why these two variables induce different responses in the crystalline state [8].

Metal-ligand bonds in transition metal complexes have been found to be more sensitive to pressure than covalent bonds in organic materials [9], leading to changes in coordination number [10–12], bond angles [13] and conformation [14]. This makes high pressure a very valuable tool for exploring the relationship between structure and physical properties in coordination compounds including magnetism [15, 16], colour [17, 18], spin state [19, 20] and absorption characteristics of metal-organic frameworks [21–23].

The pressure-sensitivity of intramolecular geometry in coordination complexes raises the question of how the compressibility of coordination bonds compares to that of intermolecular interactions such as hydrogen bonds. $[Ni(en)_3][NO_3]_2$ is an ideal candidate for this kind of study since it contains both kinds of interaction. No studies have been conducted on $[Ni(en)_3][NO_3]_2$ under high-pressure conditions. The aim of this work is therefore to determine the behaviour of $[Ni(en)_3][NO_3]_2$ under pressure with the aims of (i) comparing the effects of high pressure with those of low temperature and (ii) comparing the compressibility of metal-ligand coordination bonds with those of hydrogen bonds.

2 Experimental

2.1 Sample preparation

$[Ni(en)_3][NO_3]_2$ was synthesized and crystallized following the literature method [6]. Different $[Ni(en)_3][NO_3]_2$ crystals were used for pressure experiments for data collections with synchrotron radiation at Diamond Light Source and with a conventional lab-source at the University of Edinburgh.

2.2 Apparatus

The high pressure studies utilized a Merrill-Bassett DAC [24], with an opening angle of 40°, 600 μm culet Boehler-Almax cut diamonds, tungsten-carbide backing discs and tungsten gasket [25]. 4 : 1 methanol-ethanol was used as the hydrostatic medium. High-pressure single crystal X-ray diffraction measurements were carried-out on a three-circle Bruker APEX diffractometer with MoKα radiation monochromated with a TRIUMPH curved-crystal monochromator and with synchrotron radiation at the Diamond Light Source on beamline I19-EH1 using radiation of wavelength 0.48590 Å and a four-circle Crystal Logic diffractometer equipped with a Rigaku Saturn CCD detector. The pressure was measured using the ruby fluorescence method [26]. Data collection strategies were as described by Dawson et al. [27].

In Section 3, below, structural analyses are based on the synchrotron data-sets; data collected using the conventional lab source were utilized for determination of lattice parameters and phase identification.

2.3 Data processing

Cell indexing and integration were carried out using the Bruker APEX II [28] software with dynamic masks generated by ECLIPSE [27]. Absorption corrections were carried out using SADABS [29]. Structures were solved by charge-flipping [30] using SUPERFLIP [31]. Distance and angle restraints were derived from the ambient-pressure structure determination and applied to the positions of non-metal atoms, but not to distances or angles involving the nickel atom. Merging and refinement of the data were performed using CRYSTALS [32]. All structures were refined against $|F|$ with reflections with $|F| < 4\sigma(|F|)$ omitted. Atomic scattering factors for the synchrotron data were calculated using FPRIME [33]. Crystal and refinement of data are recorded in Table 1.

2.4 Structural analysis

Analysis of the bonding interactions was conducted using the program PLATON [34] while MERCURY [35] and

Tab. 1: Crystal data

Pressure (GPa)	0.13	0.87	1.93
λ (Å)	0.4859	0.4859	0.4859
Sin θ/λ (Å)	0.7	0.7	0.7
Crystal System	Hexagonal	Hexagonal	Hexagonal
Space Group	$P6_322$	$P6_122$	$P6_122$
a/b (Å)	8.8403(6)	8.7393(4)	8.6308(4)
c (Å)	11.2668(8)	32.9084(17)	32.2623(16)
V (Å^3)	762.54(9)	2176.66(18)	2081.27(17)
Z	2	6	6
D_{calc} (Mg m^{-3})	1.58	1.66	1.74
Reflections	6809	18938	18407
Unique Reflections	833	2174	2102
R_{int}	0.055	0.061	0.048
R	0.0243	0.0329	0.0250
R_w	0.0302	0.0438	0.0272
GooF	1.0050	1.1424	1.0162
Data/Parameters	702/34	1784/97	1734/97
Flack Parameter	−0.05(7)	−0.02(7)	−0.01(4)
ρ_{max}/ρ_{min} (e · Å^{-3})	0.21/−0.13	0.39/−0.28	0.32/−0.25

DIAMOND [36] were utilized for visualization. Calculation of interstitial voids was carried-out using the contact surface algorithm in MERCURY, a probe radius of 0.5 Å and a grid spacing of 0.1 Å. Searches of the Cambridge Structural Database v 5.32 [37] employed the program CONQUEST v 1.13. ISODISTORT v 5.4.5 [38] was used for symmetry-mode analysis; the animation of the distortion mode available in the supplementary material was produced with GIMP v 2.8.2 [39] using frames generated with ISODISTORT.

2.5 Differential scanning calorimetry

DSC data were collected at the Durham University Chemistry Department using a Perkin Elmer DSC 8500 instrument. The sample was contained in a sealed aluminium pan, with an empty pan as a reference. The scan rate was 10 K min^{-1}.

3 Results

3.1 General comments

The crystal structure of $[Ni(en)_3][NO_3]_2$ has been determined at ambient temperature up to a pressure of 1.93 GPa. Beyond 1.93 GPa data quality deteriorated with substantial broadening of diffraction peaks and loss of high-resolution data, possibly ascribable to the on-set of amorphisation.

The crystal system remains hexagonal throughout the pressure range studied. The change in unit cell parameters in response to pressure is presented in Fig. 1. In order to place the values for phases I and II on a comparable scale, the *c* axis length in Fig. 1b and cell volume in Fig. 1 have been divided by *Z* (2 for phase I and 6 for phase II). The data shown in the plot were collected using a lab source, and numerical values of the parameters plotted are available in the supplementary material (Table S1). The *c*-axis and volume plots show small discontinuities between 0.82 and 1.02 GPa, indicative of the phase transition. Observation of phase II in the synchrotron study at 0.87 GPa enables us to bracket the transition pressure between 0.82 and 0.87 GPa.

The phase transition leads to a tripling of the unit cell *c*-axis and a change in symmetry from $P6_322$ (phase I) to $P6_122$ or $P6_522$ (phase II). The complex spontaneously resolves into enantiopure crystals of the Δ or Λ forms on crystallisation from solution, and the space group obtained for phase-II depends on the enantiomorph of phase (I), Δ giving $P6_522$ and Λ giving $P6_122$. The same dependence is observed for the low-temperature phase transition [6]. It occurs because the inverted image of a structure in $P6_322$ also has space group $P6_322$, whereas $P6_122$ and $P6_522$ form an enantiomorphic pair and formation of an inverted im-

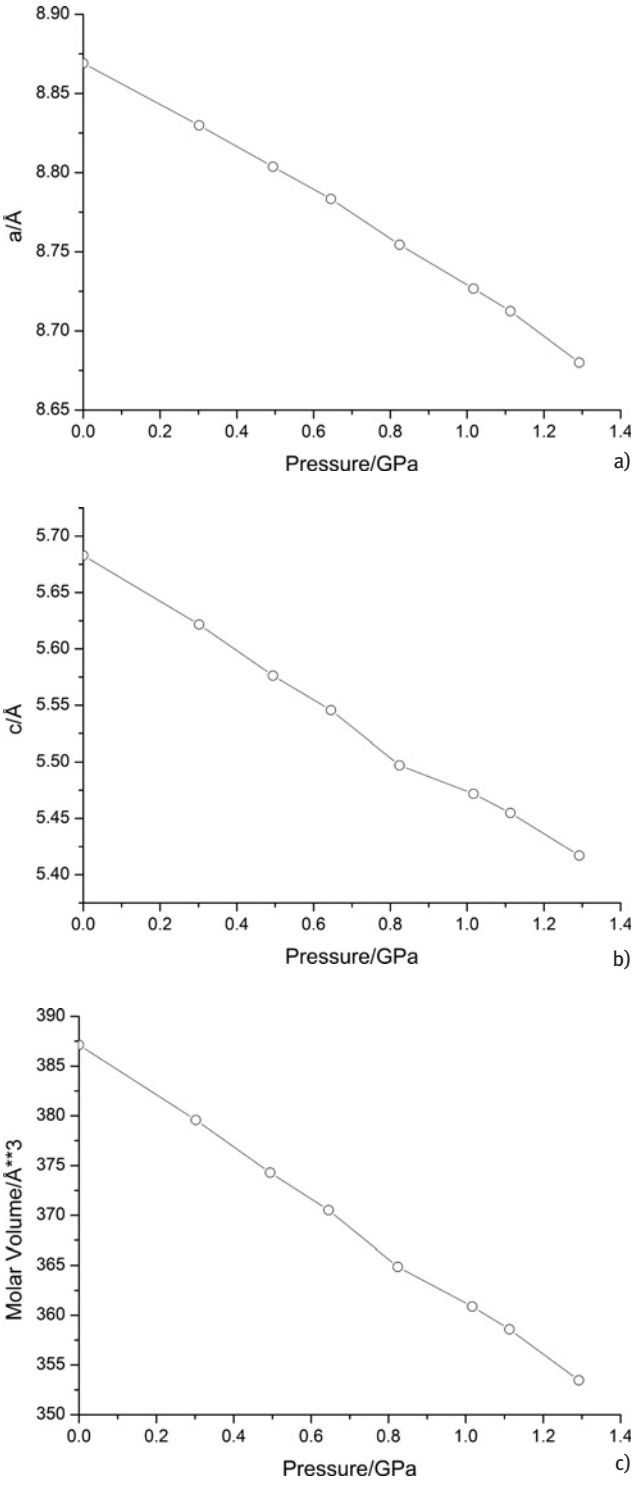

Fig. 1: Trends in (a) *a*-axis length, (b) *c*-axis length and (c) molecular volume with pressure.

age implies a change of space group from one member of the pair to the other. In the following discussion we make the assumption that the effects seen on compression do not depend on the enantiomorph of the sample.

The same transition from phase I to II has been found to occur at ~109 K and ambient pressure by diffraction measurements. As part of this work a differential scanning calorimetry trace was measured, and this showed an endotherm centred at 108 K as temperature was scanned from 99 K to 150 K (see supplementary material, Fig. S1). The width of the transition is similar to that seen in Fig. 3 in Farrugia et al.'s paper [6]. The enthalpy change for the transition is 142 J mol^{-1}, and the entropy change 1.32 J mol^{-1} K^{-1}. Though small, the non-zero values for these quantities show that the transition is first order. This is in agreement with the conclusion drawn by Farrugia et al. on the basis of the shapes of plots of cell dimensions and volume against temperature and the large displacements of molecular centres of gravity which occur at the transition.

3.2 Response of the nickel coordination environment to pressure

The nickel atom in $[Ni(en)_3][NO_3]_2$ is six coordinate with a distorted octahedral NiN_6 coordination environment (Fig. 2). In phase I (Fig. 2a) the metal atom occupies a site of 3.2 point symmetry which makes all six Ni–N bonds symmetry equivalent with a distance of 2.1309(17) Å observed at 0.13 GPa (Table 2). This compares to 2.1362(4) Å at 123 K [6]. The bond angles vary between 82.04(7)° and 93.41(7)°.

In phase II (Fig. 2b) there are three unique Ni–N interactions. At 1.93 GPa the Ni–N bonds have a range of 2.1171(18)–2.1297(15) Å; in phase II at 100 K the range is 2.1345(5)–2.1389(5) Å, indicating that pressure has a modest effect on metal-ligand distances. Though the C–C distances in the ethylenediamine ligands appear to increase in length in phase II (Table 2), this is likely a consequence of diminished thermal motion at elevated pressure (U_{eq}(C) = 0.054 Å^2 at 0.13 GPa and 0.036–0.041 Å^2 at 0.87 GPa).

The maximum change in N–Ni–N bond angle and NCCN torsion angle are 1.88(9)° (N1–Ni1–N3) and 1.8(4)° (N2–C21–C31–N3), respectively.

3.3 Response of hydrogen bonds to pressure

In phase I at 0.13 GPa Ni1 of the cations and N4 of the anions are distributed along the same three-fold axes

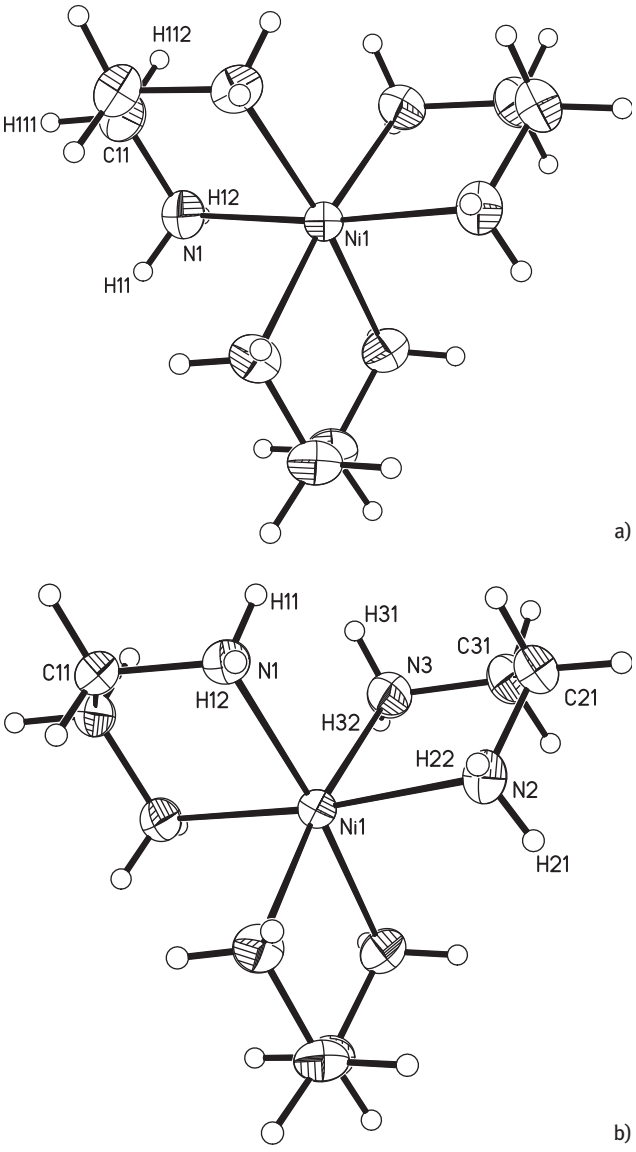

Fig. 2: Structures of $[Ni(en)_3]^{2+}$ at (a) 0.13 GPa and (b) 0.87 GPa showing atom numbering. Thermal ellipsoids enclose 50% probability surfaces.

Tab. 2: Intramolecular bond lengths (Å) as a function of pressure.

Phase I		Phase II		
Pressure (GPa)	**0.13**		**0.87**	**1.93**
Ni1–N1	2.1309(13)	Ni1–N1	2.130(2)	2.1232(14)
		Ni1–N2	2.127(2)	2.1171(15)
		Ni1–N3	2.134(2)	2.1297(13)
N1–C11	1.477(2)	N1–C11	1.474(3)	1.474(2)
		N2–C21	1.474(3)	1.481(2)
		N2–C31	1.461(3)	1.472(2)
C11–C11^{i}	1.487(4)	C11–C11^{ii}	1.522(5)	1.515(3)
		C21–C31	1.503(4)	1.510(2)

^{i} $-x+y, y, -z+{}^{3}/_{2}$
^{ii} $-y+1, -x+1, -z+{}^{5}/_{6}$

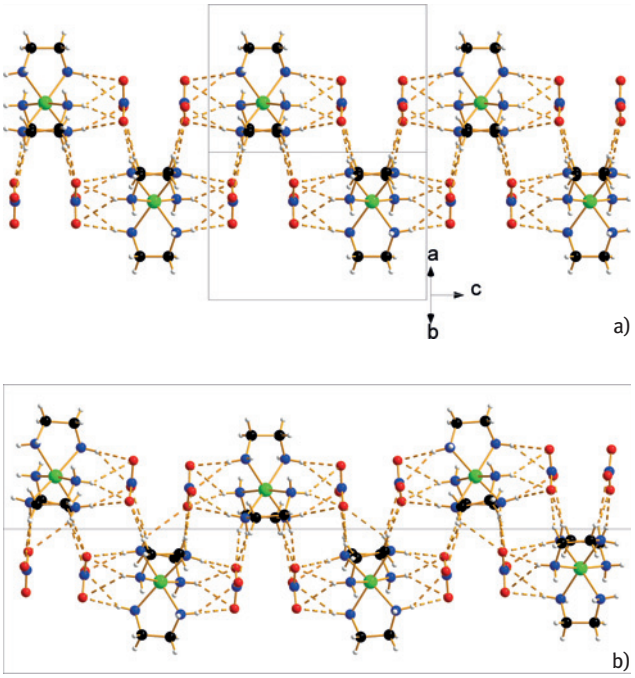

Fig. 3: (a) Phase I at 0.13 GPa and (b) phase II at 0.87 GPa viewed perpendicular to (110), showing hydrogen bonding. Colour scheme: Ni green, O red, N blue, C black and H white. The scale of both figures is the same.

running parallel to ***c***. Pairs of anions are located above and below the upper and lower faces of the cation octahedra, interacting through bifurcated N1–H12…O41 H-bonds (Fig. 3a). The bifurcation is unsymmetrical with H12…O41 distances of 2.22 and 2.57 Å (Table 3, NH distances normalised to 1.01 Å). These units are stacked along ***c*** with pairs of anions facing one another. When viewed along ***c*** these pairs of nitrates are staggered relative to each other, but with N…N distances of 3.130(3) Å (Fig. 4a). This apparently unfavourable electrostatic interaction is stabilised by inter-stack N1–H11…O41 H-bonds formed in layers parallel to the *ab* face of the unit cell. These contacts are also bifurcated with H11…O41 distances measuring 2.30 and 2.68 Å. The 'diagonal' distance between H11 and O41 in the nitrate anion directly below that forming the primary H-bonds to the cation is 3.20 Å.

The transition from phase I to II modifies the orientations of the cations and anions. Over the course of the phase transition, the point symmetries of the cations and anions are reduced from 3.2 to ..2 and 3 to 1, respectively, breaking the three-fold degeneracy of the intra and inter-stack interactions. Phase II is thus a distorted version of phase I, consisting of the same intra- and inter-stack interactions described above, but with the set of four independent bifurcated NH…O interactions of phase I developing into twelve independent interactions in phase II (Figs. 3b and 4b).

Related interactions in phases I and II are correlated in Table 3. The O…H distances forming the shorter components of the bifurcated intra-stack H-bonds change by up to 8.56%, whilst the longer interactions in the same stack change by up to 5.45% from 0.13 to 1.93 GPa, so that the bifurcation becomes more unsymmetrical. Similarly the shorter O…H interstack distances change by up to 8.26%, whilst the longer interactions change by up to 7.09% over the same pressure range. The greatest change in O…H distances occurs for the diagonal H11…O41 hydrogen bond, which contracts by 24% from 3.20 Å to 2.43 Å at 1.93 GPa. This substantial change is a consequence of the shift in the nitrate positions during the phase transition. This shift, which can be seen by comparing Fig. 3a and b, is clearest in an animation of the displacements during the transition which is available in the supplementary material (Fig. S2).

The short N…N distance formed between nitrate anions is 3.130(3) Å at 0.13 GPa. After the transition to

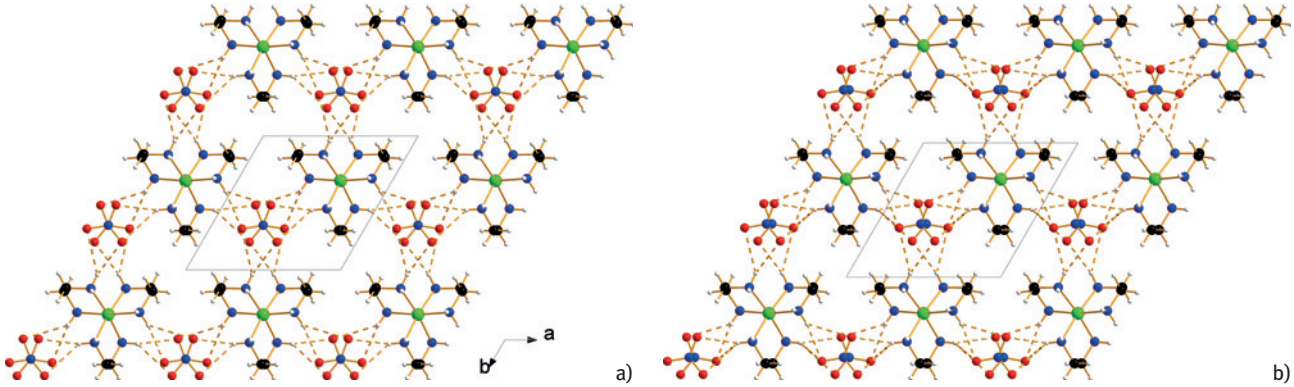

Fig. 4: Hydrogen bonding network viewed along **c** in (a) phase I at 0.13 GPa and (b) phase II at 0.87 GPa. The colour scheme is the same as Fig. 3.

Tab. 3 Normalized hydrogen bond lengths/angles as a function of pressure.

Phase I[a]		**Phase II**[b]			
Pressure (GPa)	**0.13**		**0.87**	**1.93**	**% Change**
Intrastack H-bonds					
N1–H12 ... O41 (Å)	3.170(2)[i]	N1–H12 ... O43 (Å)	3.106(3)	3.0510(19)	3.74
H12 ... O41 (Å)	2.22	H12 ... O43 (Å)	2.17	2.14	3.60
<N1–H12 ... O41 (°)	156	<N1–H12 ... O43 (°)	153	149	4.49
		N2–H22 ... O41 (Å)	3.157(3)	3.143(2)	0.83
		H22 ... O41 (Å)	2.21	2.18	1.80
		<N2–H22 ... O41 (°)	156	158	−1.28
		N3–H32 ... O42 (Å)	3.071(3)[i]	3.0153(19)	4.87
		H32 ... O42 (Å)	2.10	2.03	8.56
		<N3–H32 ... O42 (°)	162	164	−5.13
N1–H12 ... O41 (Å)	3.431(2)[ii]	N1–H12 ... O41 (Å)	3.358(3)	3.306(2)	3.64
H12 ... O41 (Å)	2.57	H12 ... O41 (Å)	2.47	2.43	5.45
<N1–H12 ... O41 (°)	143	<N1–H12 ... O41 (°)	146	148	−3.49
		N3–H32 ... O43 (Å)	3.341(3)[i]	3.305(2)	3.67
		H32 ... O43 (Å)	2.52	2.53	1.56
		<N3–H32 ... O43 (°)	137	133	7.00
		N2–H22 ... O42 (Å)	3.451(3)	3.439(2)	−0.23
		H22 ... O42 (Å)	2.60	2.59	−0.78
		<N2–H22 ... O42 (°)	141	141	1.40
Interstack H-bonds					
N1–H11 ... O41 (Å)	3.229(3)[iii]	N1–H11 ... O41 (Å)	3.198(4)[ii]	3.171(2)	1.80
H11 ... O41 (Å)	2.30	H11 ... O41 (Å)	2.40	2.36	−2.61
<N1–H11 ... O41 (°)	152	<N1–H11 ... O41 (°)	135	136	10.53
		N3–H31 ... O42 (Å)	3.149(4)[iii]	3.098(3)	4.01
		H31 ... O42 (Å)	2.16	2.11	8.26
		<N3–H31 ... O42 (°)	165	167	−9.87
		N2–H21 ... O43 (Å)	3.197(4)[iv]	3.162(2)	2.08
		H21 ... O43 (Å)	2.27	2.22	3.48
		<N2–H21 ... O43 (°)	153	156	−2.63
N1–H11 ... O41 (Å)	3.455(3)[v]	N1–H11 ... O43	3.397(3)[ii]	3.335(2)	3.47
H11 ... O41 (Å)	2.68	H11 ... O43	2.70	2.61	2.61
<N1–H11 ... O41	137	<N1–H11 ... O43	126	129	5.84
		N3–H31 ... O41 (Å)	3.367(4)[iii]	3.298(3)	4.55
		H31 ... O41 (Å)	2.55	2.49	7.09
		<N3–H31 ... O41 (°)	137	136	0.73
		N2–H21 ... O42	3.411(5)[iv]	3.364(3)	2.63
		H21 ... O42	2.61	2.53	5.60
		<N2–H21 ... O42	136	139	−1.46
Diagonal					
N1–H11 ... O41	3.830(3)[vi]	N1–H11 ... O42 (Å)	3.382(3)[iii]	3.181(2)	16.96
H11 ... O41 (Å)	3.20	H11 ... O42 (Å)	2.59	2.43	24.06
<N1–H11 ... O41 (°)	128	< N1–H11 ... O42 (°)	135	131	−2.34

[a] Symmetry operations: (i) $y, 1-x+y, -^1/_2+z$; (ii) $x-y, x, -^1/_2+z$; (iii) $x, x-y, ^3/_2-z$; (iv) $x, x-y, ^3/_2-z$; (v) $1-x+y, y, ^3/_2-z$; (vi) $1-x+y, 1-x, z$.

[b] Symmetry operations: (i) $1-y, 1-x, ^5/_6-z$; (ii) $1+x-y, 2-y, -1-z$; (iii) $y, 1-x+y, -^1/_6+z$; (iv) $1+x-y, 1-y, 1-z$

phase II this decreases to 3.026(3) Å at 0.87 GPa and 2.9704(18) Å at 1.9 GPa.

Interstitial voids in the crystal structure are displayed in Fig. 5. The interstitial void volume per formula unit is 60.56 Å^3 at 0.13 GPa, 40.00 Å^3 at 0.87 GPa, and 26.37 Å^3 at 1.93 GPa, representing 15.9 %, 11.0 %, and 7.6 % of the total unit cell volume respectively. The largest and most persistent of the interstitial voids in phase I have an approximately oblate shape with the long principal axes in the *ab* plane, and the short axis parallel to *c*.

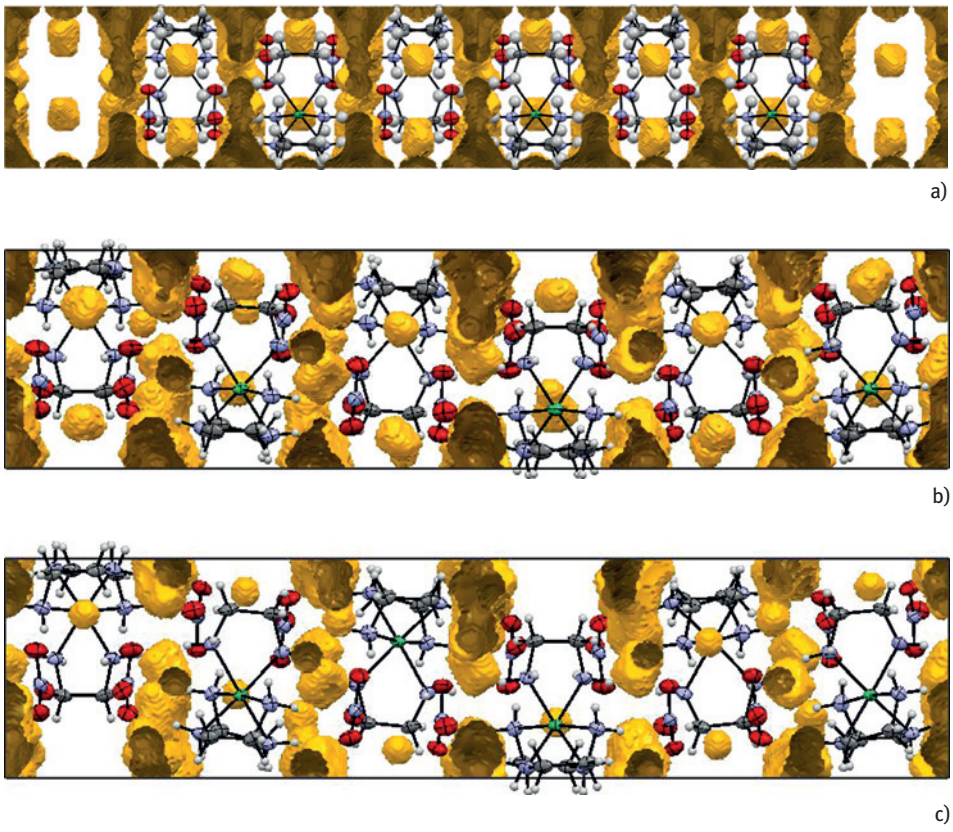

Fig. 5: Interstitial voids (yellow) at 0.13 (phase I), 0.87 (phase II), and 1.93 GPa (phase II) viewed along ***a***.

4 Discussion

4.1 Distortion analysis

The phase transition from phase I to phase II between 0.82 GPa and 0.87 GPa is similar to that observed by Farrugia et al. [6] at 109 K. From the discontinuities present in Fig. 1b and c it seems reasonable to infer that the transition at high pressure is also first order.

Symmetry mode analysis based on the Ni, N and O positions of phase I at ambient pressure and phase II and 0.87 GPa (ISODISTORT) shows that the structure evolves via a displacive mechanism in which two modes (corresponding to irreducible representations Γ_1 and Δ_6) are active. The first of these represents the contraction of the structure with pressure; the second corresponds to rotations of the cations and anions in which the magnitudes of the rotations vary in a wave-like fashion along the *c*-direction of the unit cell. This mode is illustrated in an animation available in the supplementary material (Fig. S2).

The displacements revealed by symmetry mode analysis can be interpreted in the context of the distribution of interstitial voids. The largest voids in phase I at ambient pressure are distributed between the layers illustrated in Fig. 5 at the points where ethylenediamine ligands in neighbouring layers meet. The reduction in symmetry enables the cations and anions to reorient and access these voids. The reorientation of the anions, which sit directly above one another in phase I, also leads to a small displacement of like-charged atoms away from one another, reducing electrostatic repulsion.

The distribution of voids is also consistent with the anisotropy of the contraction of the unit cell parameters. The greatest contraction occurs along [001], with the value of c/Z decreasing by 5.38% over the pressure series; c/Z also undergoes a larger contraction than the *a*-axis length as a result of the phase transition (2.64% versus 1.14%), corresponding to flattening of the large oblate voids described above (Fig. 5). Movement of the structure along the *a* and *b* axes is hindered by the lack of void space between the stacks.

4.2 Effect of pressure on H-bonding

One of the aims of this work was to compare the compressibility of Ni–N and NH ... O H-bonds, which are both present in the structure of $[Ni(en)_3][NO_3]_2$. The maximum compression seen for the Ni–N bond distance was

0.014(2) Å, but 0.19 Å for the O…H distances. The compression in the H-bond distances is thus an order of magnitude greater. This effect is unlikely to be a simple effect of bond strength. The Cu–N bond energies in copper(II) ammine complexes have been estimated to be between 90 and 180 kJ mol^{-1} [40], and the values for Ni–N bonds are likely to be similar; the intermolecular interactions mediated by charge-assisted H-bonds in $[Ni(en)_3][NO_3]_2$ likely have similar energies (cf. similar charge-assisted interactions in amino acids have energies of up to 150 kJ mol^{-1}) [41].

The geometry of the H-bonds in $[Ni(en)_3][NO_3]_2$ can be compared to those found in similar structures. The frequency distribution for the NH…O distance in metal-bound NH…nitrate H-bonds in the CSD is shown in Fig. 6a and has a maximum frequency where the NH…O distance is 2.08 Å. The hydrogen bond lengths calculated for phase-I at 0.13 GPa correspond to those structures that reside in the 2.20–2.30 Å region of the histogram, demonstrating a potential for compression. Compression

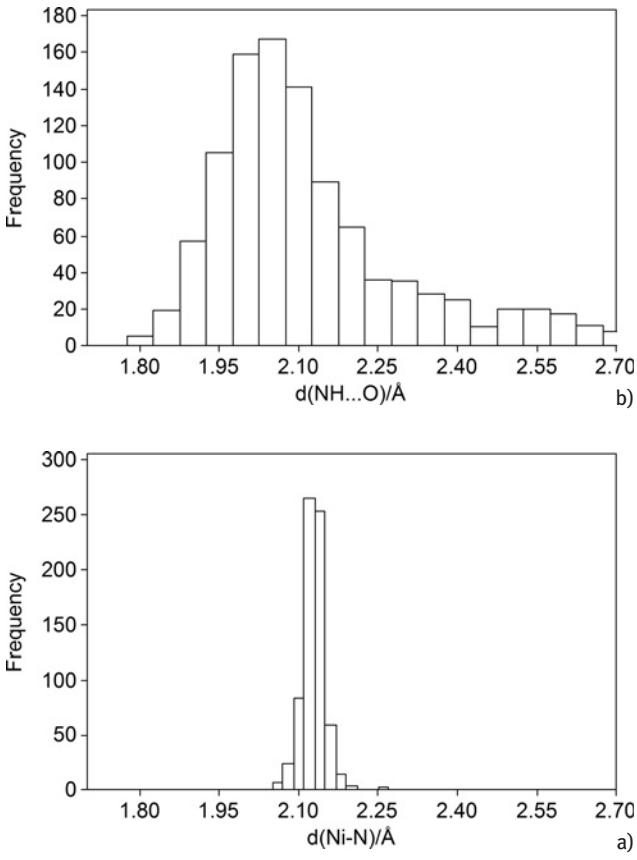

Fig. 6: Histograms of (a) normalised NH…O H-bond distances involving metal-bound amino and nitrate moieties and (b) Ni–N distances in six coordinate nickel complexes. CSD search criteria were: *R* factor ≤5%, 3D coordinates determined, no errors, no disorder. Both plots have the same horizontal scale.

of the hydrogen bonding network can be compared to pressure trends observed in the amino acids. NH…O distances in *L*-cysteine [42] undergo a reduction in length by up to 5.4% from ambient pressure to 1.8 GPa. In *L*-alanine [41], for example, some of the NH…O interactions decrease in length by up to 4.3% from ambient pressure to 2.30 GPa while other hydrogen bonds demonstrate very little change over the same pressure range. When the pressure is increased to 13.60 GPa the same interactions undergo a compression of up to 9.74%. In $[Ni(en)_3][NO_3]_2$ the majority of hydrogen bonds therefore undergo compression similar to that observed in the amino acids.

A characteristic of the H-bond distributions described above, and exemplified by that in Fig. 6a, is that they are very broad compared to a histogram on Ni–N distances in octahedral nickel complexes (Fig. 6b). This points to a much flatter potential energy versus distance surface for H-bonds than for Ni–N bonds, and this explains why H-bonds are the more sensitive to pressure. Coordination bonds with flatter potentials, such as elongated Cu–N or O bonds in Jahn-Teller distorted Cu(II) complexes, show much greater sensitivity to pressure [12, 15, 16, 18]. The response of structures under pressure is also to minimise free energy by packing molecules more efficiently, and reducing interstitial voids. This naturally also affects intermolecular interactions to a greater extent than intramolecular bonds.

5 Conclusion

We have shown that $[Ni(en)_3][NO_3]_2$ undergoes a phase transition between 0.82 and 0.87 GPa in which the structure undergoes a distortion involving rotations of the cations and anions leading to a tripling of the unit cell volume. The structure remains in this phase up to 1.93 GPa. Previous work had shown that the same transition occurs on cooling the crystal at ambient pressure below 109 K. While most intermolecular H-bonding interactions shorten by around 5% between ambient pressure and 1.93 GPa, the reorientations of the cations and anions during the phase transition shorten one such interaction by almost 0.8 Å, or 24%. The compression in Ni–N distances is an order of magnitude less than that seen for the H-bonds. CSD searches indicate that this reflects the shape of the H-bonding and Ni–N bonding interatomic potentials.

Acknowledgements: We thank Diamond Light Source and EPSRC for studentship funding to CAC, and the for-

mer also for provision of synchrotron beamtime. We also thank Mr Douglas Carswell of the Durham University Chemistry Department for collection of DSC data.

References

[1] L. N. Swink, M. Atoji, The Crystal Structure of Triethylenediaminenickel(II) Nitrate, $Ni(NH_2CH_2CH_2NH_2)_3(NO_3)_2$. *Acta Cryst.* **1960**, *13*, 639–643.

[2] P. Macchi, H.-B. Bürgi, A. S. Chimpri, J. Hauser, Z. Gál, Low-energy contamination of Mo microsource X-ray radiation: analysis and solution of the problem. *J. Appl. Cryst.* **2011**, *44*, 763–771.

[3] E. V. Boldyreva, T. N. Drebushchak, T. P. Shakhtshneider, H. Sowa, H. Ahsbahs, S. V. Goryainov, S. N. Ivashevskaya, E. N. Kolesnik, V. A. Drebushchak, E. B. Burgina, Variable-temperature and variable-pressure studies of small-molecule organic crystals. *Arkivoc* **2004**, 128–155.

[4] A. E. Goeta, J. A. K. Howard, Low temperature single crystal X-ray diffraction: advantages, instrumentation and applications. *Chem. Soc. Rev.* **2004**, *33*, 490–500.

[5] A. Katrusiak, High-pressure crystallography. *Acta Cryst.* **2008**, *A64*, 135–148.

[6] L. J. Farrugia, P. Macchi, A. Sironi, Reversible displacive phase transition in $[Ni(en)_3]^{2+}(NO_3^-)_2$: a potential temperature calibrant for area-detector diffractometers. *J. Appl. Cryst.* **2003**, *36*, 141–145.

[7] S. A. Moggach, S. Parsons, P. A. Wood, High-pressure polymorphism in amino acids. *Cryst. Rev.* **2008**, *14*, 143–184.

[8] E. V. Boldyreva, High-pressure diffraction studies of molecular organic solids. A personal view. *Acta Cryst.* **2008**, *A64*, 218–231.

[9] S. A. Moggach, S. Parsons, High pressure crystallography of inorganic and organometallic complexes. *Specialist Periodic Reports: Spectroscopic Properties of Inorganic and Organometallic Compounds* **2009**, *40*, 324–354.

[10] D. R. Allan, A. J. Blake, D. Huang, T. J. Prior, M. Schroeder, High pressure co-ordination chemistry of a palladium thioether complex: pressure versus electrons. *Chem. Comm.* **2006**, 4081–4083.

[11] S. A. Moggach, K. W. Galloway, A. R. Lennie, P. Parois, N. Rowantree, E. K. Brechin, J. E. Warren, M. Murrie, S. Parsons, Polymerisation of a Cu(II) dimer into 1D chains using high pressure. *CrystEngComm* **2009**, *11*, 2601–2604.

[12] A. Prescimone, C. Morien, D. Allan, J. A. Schlueter, S. W. Tozer, J. L. Manson, S. Parsons, E. K. Brechin, S. Hill, Pressure-Driven Orbital Reorientations and Coordination-Sphere Reconstructions in $[CuF_2(H_2O)_2(pyz)]$. *Angew. Chem., Int. Ed. Engl.* **2012**, *51*, 7490–7494.

[13] G. M. Espallargas, L. Brammer, D. R. Allan, C. R. Pulham, N. Robertson, J. E. Warren, Noncovalent interactions under extreme conditions: high-pressure and low-temperature diffraction studies of the isostructural metal-organic networks $(4\text{-chloropyridinium})_2[CoX_4]$ (X = Cl, Br). *J. Am. Chem. Soc.* **2008**, *130(28)*, 9058–9071.

[14] N. Casati, P. Macchi, A. Sironi, Staggered to eclipsed conformational rearrangement of $[Co_2(CO)_6(PPh_3)_2]$ in the solid state: An X-ray diffraction study at high pressure and low temperature. *Angew. Chem., Int. Ed. Engl.* **2005**, *44*, 7736–7739.

[15] P. Parois, S. A. Moggach, J. Sanchez-Benitez, K. V. Kamenev, A. R. Lennie, J. E. Warren, E. K. Brechin, S. Parsons, M. Murrie, Pressure-induced Jahn-Teller switching in a Mn_{12} nanomagnet. *Chem. Comm.* **2010**, *15*, 1881–1883.

[16] A. Prescimone, C. J. Milios, S. A. Moggach, J. E. Warren, A. R. Lennie, J. Sanchez-Benitez, K. Kamenev, R. Bircher, M. Murrie, S. Parsons, E. K. Brechin, $[Mn_6]$ under pressure: a combined crystallographic and magnetic study. *Angew Chem Int Ed Engl* **2008**, *47*, 2828–2831.

[17] P. J. Byrne, P. J. Richardson, J. Chang, A. F. Kusmartseva, D. R. Allan, A. C. Jones, K. V. Kamenev, P. A. Tasker, S. Parsons, Piezochromism in nickel salicylaldoximato complexes: tuning crystal-field splitting with high pressure. *Chem. Eur. J.* **2012**, *18*, 7738–7748.

[18] K. W. Galloway, S. A. Moggach, P. Parois, A. R. Lennie, J. E. Warren, E. K. Brechin, R. D. Peacock, R. Valiente, J. Gonzalez, F. Rodriguez, S. Parsons, M. Murrie, Pressure-induced switching in a copper(II) citrate dimer. *CrystEngComm* **2010**, *12*, 2516–2519.

[19] T. Granier, B. Gallois, J. Gaultier, J. A. Real, J. Zarembowitch, High-pressure single-crystal X-ray diffraction study of two spin-crossover iron(II) complexes: $Fe(Phen)_2(NCS)_2$ and $Fe(Btz)_2(NCS)_2$. *Inorg. Chem.* **1993**, *32*, 5305–5312.

[20] P. Guetlich, A. B. Gaspar, Y. Garcia, V. Ksenofontov, Pressure effect studies in molecular magnetism. *Comptes Rendus Chimie* **2007**, *10*, 21–36.

[21] A. J. Graham, D. R. Allan, A. Muszkiewicz, C. A. Morrison, S. A. Moggach, The effect of high pressure on MOF-5: guest-induced modification of pore size and content at high pressure. *Angew. Chem., Int. Ed. Engl.* **2011**, *50*, 11138–11141.

[22] A. J. Graham, J.-C. Tan, D. R. Allan, S. A. Moggach, The effect of pressure on Cu-btc: framework compression vs. guest inclusion. *Chem. Comm.* **2012**, *48*, 1535–1537.

[23] S. A. Moggach, T. D. Bennett, A. K. Cheetham, The effect of pressure on ZIF-8: increasing pore size with pressure and the formation of a high-pressure phase at 1.47 GPa. *Angew. Chem., Int. Ed. Engl.* **2009**, *48*, 7087–7089.

[24] L. Merrill, W. A. Bassett, Miniature diamond anvil pressure cell for single-crystal X-ray-diffraction studies. *Rev. Sci. Instruments* **1974**, *45*, 290–294.

[25] S. A. Moggach, D. R. Allan, S. Parsons, J. E. Warren, Incorporation of a new design of backing seat and anvil in a Merrill–Bassett diamond anvil cell. *J. Appl. Cryst.* **2008**, *41*, 249–251.

[26] G. J. Piermarini, S. Block, J. D. Barnett, R. A. Forman, Calibration of the pressure dependence of the R1 ruby fluorescence line to 195 kbar. *J. Appl. Phys.* **1975**, *46*, 2774–2780.

[27] A. Dawson, D. R. Allan, S. Parsons, M. Ruf, Use of a CCD diffractometer in crystal structure determinations at high pressure. *J. Appl. Cryst.* **2004**, *37*, 410–416.

[28] Bruker. APEX 2. *Bruker AXS Inc., Madison, Wisconsin, USA* **2001**.

[29] G. M. Sheldrick, SADABS. 2008-1 ed.; Bruker AXS Inc., Madison, Wisconsin, USA, 2008.

[30] G. Oszlanyi, A. Süto, Ab initio structure solution by charge flipping. *Acta Cryst.* **2004**, *A60*, 134–141.

[31] L. Palatinus, Chapuis, G. SUPERFLIP. A computer program for the solution of crystal structures by charge flipping in arbitrary dimensions. *J. Appl. Cryst.* **2007**, *40*, 786–790.

[32] P. W. Betteridge, J. R. Carruthers, R. I. Cooper, K. Prout, D. J. Watkin, CRYSTALS version 12: software for guided crystal structure analysis. *J. Appl. Cryst.* **2003**, *36*, 1487.

[33] L. Kissel, R. H. Pratt, Corrections to tabulated anomalous-scattering factors. *Acta Cryst*. **1990**, *A46*, 170–175.
[34] A. L. Spek, Single-crystal structure validation with the program PLATON. *J. Appl. Cryst*. **2003**, *36*, 7–13.
[35] C. F. Macrae, I. J. Bruno, J. A. Chisholm, P. R. Edgington, P. McCabe, E. Pidcock, L. Rodriguez-Monge, R. Taylor, J. van de Streek, P. A. Wood, Mercury CSD 2.0 – new features for the visualization and investigation of crystal structures. *J. Appl. Cryst*. **2008**, *41*, 466–470.
[36] K. Brandenburg, DIAMOND. Crystal Impact GbR: Bonn, 1999.
[37] F. H. Allen, The Cambridge Structural Database: a quarter of a million crystal structures and rising. *Acta Cryst*. **2002**, *B58*, 380–388.
[38] B. J. Campbell, H. T. Stokes, D. E. Tanner, D. M. Hatch, ISODISPLACE: a web-based tool for exploring structural distortions. *J. Appl. Cryst*. **2006**, *39*, 607–614.
[39] S. Kimball, P. Mattis, GIMP. 2.8.2 ed.: Berkeley, California, USA, 1995.
[40] A. Nimmermark, L. Öhrström, J. Reedijk, Metal-ligand bond lengths and strengths: are they correlated? A detailed CSD analysis. *Z. Krist* **2013**, *228*, 311–317.
[41] N. P. Funnell, A. Dawson, D. Francis, A. R. Lennie, W. G. Marshall, S. A. Moggach, J. E. Warren, S. Parsons, The effect of pressure on the crystal structure of *L*-alanine. *CrystEngComm* **2010**, *12*, 2573–2583.
[42] S. A. Moggach, D. R. Allan, S. J. Clark, M. J. Gutmann, S. Parsons, C. R. Pulham, L. Sawyer, High-pressure polymorphism in *L*-cysteine: the crystal structures of *L*-cysteine-III and *L*-cysteine-IV. *Acta Cryst*. **2006**, *B62*, 296–309.

Received August 12, 2013; accepted October 22, 2013
Published online January 10, 2014